# Low-Complexity Deadbeat Model Predictive Current Control With Duty Ratio for Five-Phase PMSM Drives

Mahmoud S. R. Saeed, Wensheng Song, *Member, IEEE*, Bin Yu, and Xuesong Wu

***Abstract*—Model predictive control (MPC) is considered as a promising control strategy for power electronic converters and drive systems due to its merits of simplicity, fast-dynamic response, and multi-variable control flexibility. However, the variable switching frequency and the large computational burden represent serious problems for applying MPC in high-power multi-phase converters and drive systems. This article introduces a low-complexity model predictive current control (MPCC) for five-phase permanent magnet synchronous machine (PMSM) with constant switching frequency based on the deadbeat (DB) principles. To avoid the full enumeration process, the proposed method calculates the reference voltage vector using the DB technique, considering one-step delay compensation. The information of the reference voltage is used to select the best approximation for the reference voltage from the enhanced control set with virtual voltage vectors (V3), which eliminate the third-harmonic phase voltage and phase current components. Moreover, the optimal duty ratio is calculated to fit the selected voltage vector on the reference voltage vector. The proposed control strategy is compared with three existing MPC techniques. The effectiveness of the proposed MPCC strategy is validated using MATLAB simulation and hardware-in-the-loop results.**

***Index Terms*—Deadbeat (DB) control, five-phase permanent magnet synchronous machine (PMSM), model predictive current control (MPCC), optimal duty ratio.**

## I. Introduction

RECENTLY, multi-phase permanent magnet synchronous machines (PMSMs) have replaced the conventional three-phase ones in many applications due to their high reliability, reduced power per phase, and low torque ripples [1], [2]. Among the multiphase PMSMs, the five-phase PMSMs have attracted the attention and have been widely used in the drive systems over the recent years [3]–[5].

Model predictive control (MPC) is a control technique, which has been widely applied on power electronic converters and drive systems [6]–[9]. The basic principle of MPC is based on using the system model to predict the behavior of the controlled parameters in the future. The controller uses this information to select the optimal actuator state based on a predefined optimization criterion. Compared with conventional linear control techniques, MPC has many advantages such as simple principles, fast response, and being applicable on multi-variable and nonlinear systems [10], [11]. MPC can be classified into two main categories: continuous control set (CCS) MPC [12] and finite control set (FCS) MPC [13], [14]. CCS-MPC requires a suitable modulation technique in the control system. The FCS-MPC considers only a finite number of output states of the adopted converter, which is usually reported and used because of the elimination of the modulator and its robustness.

A salient drawback of the FCS-MPC is that it requires high sampling frequency to guarantee accurate tracking of the controlled variables, which represents high computational burden on the controller hardware. Hence, high-cost controllers are required to implement FCS-MPC in the industry. In addition, the FCS-MPC applies the optimal state of the system according to a specific cost function. Hence, it may lead to producing nonmodulated switching pulses, which have variable switching frequency. Therefore, large inductor and capacitor filters are required to remove the current and voltage harmonics [15]. Multistep MPC techniques are considered as a low power loss solution with high harmonics in MPC. However, increasing the prediction horizon will lead to high computational burden. Sphere decoding optimization algorithm has been utilized to reduce the computational burden of long-horizon MPC in [16] and [17].

For the variable switching frequency problem, many literatures have proposed MPC with constant switching frequency. Modulated model predictive control (M2PC) techniques have been proposed to combine the advantages of MPC with maintaining constant switching frequency and improved steady-state performance [18]–[21]. However, M2PC has high computational burden due to the enumeration process of the available voltage vectors with additional modulation algorithms. Constant switching frequency MPC with optimal switching sequence has been proposed in [22]. However, this technique is limited to single-phase converters. MPC with virtual voltage vectors (V3) has been proposed for three-phase PMSM drives in [23]. These virtual vectors can be generated using a modulation stage, which assures constant switching frequency operation. Adding more

Manuscript received June 18, 2019; revised December 16, 2019 and February 13, 2020; accepted March 13, 2020. Date of publication March 29, 2020; date of current version July 20, 2020. This work was supported in part by the National Key R & D Program of China under Grant 2017YFB1200900 and in part by the Fundamental Research Funds for the Central Universities under Grant 2682018QY05. Recommended for publication by Associate Editor R. Kennel. *(Corresponding author: Wensheng Song.)*

The authors are with the School of Electrical Engineering, Southwest Jiaotong University, Chengdu 610031, China (e-mail: mahmoud.said@eng.svu.edu.eg; songwsh@swjtu.edu.cn; yubin_electric@163.com; xuesong3@ualberta.ca).

Color versions of one or more of the figures in this article are available online at http://ieeexplore.ieee.org.

Digital Object Identifier 10.1109/TPEL.2020.2983048

V3 can enhance the quality of the voltage and current waveforms. However, an increased number of virtual vectors means heavy computational burden. Another FCS-model predictive current control (MPCC) with virtual vectors (FCS-MPCC-V3) has been proposed for five-phase PMSM drive in [24], and for dual three-phase machines in [25]. The FCS-MPCC-V3 uses 12 voltage vectors; 2 zero vector and 10 optimized V3 in order to eliminate the third harmonic voltage components, which reduce the third harmonics of phase currents. This method is modified by applying the virtual voltage with optimal duty ratio and applying a zero-vector for the remaining part of the sampling period in (FCS-MPCC-V3-DRO) [26]. Although the number of virtual vectors is relatively reduced compared with the conventional MPCC, a complete enumeration for testing all voltage vectors is still required. Thus, the computational burden is still high.

Regarding to the complexity problem, several solutions have been proposed to reduce the computational burden. In [27], the optimal voltage vector is selected in one subspace according to the sector information of the reference voltage vector. This method is modified to select two vectors every control interval in [28] and [29], three vector-based methods [30], and generalized multiple-vector methods in [31] and [32]. In these schemes, the reference voltage vector is calculated according to the deadbeat (DB) control principles. Another DB solution applied for model predictive torque control (MPTC) of PMSM drive has been proposed in [33]. A simplified high-quality MPTC with separate torque and flux cost functions has been proposed in [34]. Reduced complexity MPC for multilevel inverters is introduced in [35], which reduces the number of tested voltage vectors during every control interval using the adjacent vector principle. However, these low-complexity methods have been only applied on the three-phase PMSM drive system, and they have not been designed to consider the specifications of multi-phase PMSMs. Multiple-vector-based FCS-MPC with constant switching frequency has been proposed for five-phase drives [36] and six-phase drives [37]. Low-complexity MPTC with the quadratic evaluation method has been applied on five-phase PMSMs [38]. This method needs to evaluate 10 vectors from the 30 available voltage vectors. For further reduction in the computational burden, [39] has introduced a new FCS-MPTC with torque and stator flux hysteresis comparators. With the aid of these comparators and a predefined lookup table, this method selects two voltage vectors to be explored every control interval with a simplified cost function. Thus, the computational burden is significantly reduced. However, this method still needs to examine two vectors during every control interval. Therefore, the computational burden reduction in five-phase PMSM drives is still a popular issue.

In this article, a DB solution with optimal duty ratio for MPCC of five-phase PMSM is introduced to further decrease the computational burden. The proposed method removes the difficulty in applying explicit voltage vector selection in two different planes, $\alpha 1$-$\beta 1$ plane and $\alpha 3$-$\beta 3$ plane, in five-phase PMSM with the aid of V3 principles [24]. This technique calculates the reference voltage vector and selects the best approximation for the fundamental reference voltage from ten optimal V3 to be applied in the next sampling interval, since the $\alpha 3$-$\beta 3$ components are set to zero. This way, the proposed scheme selects the optimal voltage vector directly without the exploration process. Then, the duty ratio of the selected vector is calculated to reduce the error between the reference voltage vector and the selected V3. For further verification of the proposed scheme potentials, the performance of the proposed method is compared with three existing MPC techniques applied on five-phase PMSM drives; namely FCS-MPCC-V3 [24], FCS-MPCC-V3-DRO [26], and hysteresis MPTC [39] using MATLAB/Simulink modeling tool and the hardware-in-the-loop (HIL) tests. Section II illustrates the standard model of the five-phase PMSM drive system. Section III gives a review on the conventional FCS-MPC techniques. The proposed algorithm principles are explained in Section IV. Simulation and HIL results are analyzed in Sections V and VI, respectively. Finally, Section VII summarizes the conclusion.

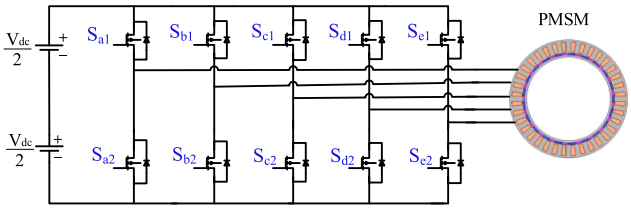


Fig. 1. Five-phase PMSM drive system using 2L-VSI.

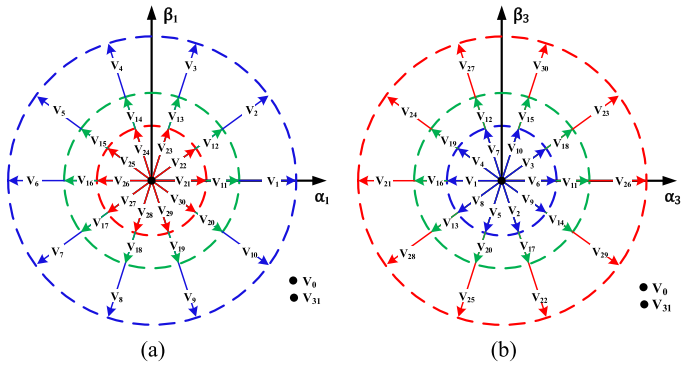


Fig. 2. Real voltage vectors of five-phase 2L-VSI in (a) $\alpha_1$-$\beta_1$ subspace, and (b) $\alpha_3$-$\beta_3$ subspace.

## II. Five-Phase PMSM Drive System Modeling

The five-phase PMSM drive system with two levels (2L) voltage source inverter (VSI) is shown in Fig. 1. The total number of the available switching states in the five-phase 2L-VSI is ($2^5 = 32$), including two zero vectors and 30 active voltage vectors, as shown in Fig. 2. The mathematical model of this system can be described as follows.

The stator voltage vector components $V_{d1}$ and $V_{q1}$, and the stator flux vector components $\psi_{d1}$, $\psi_{q1}$ of the PMSM in $d_1$-$q_1$

reference frame can be described as

$$\begin{cases} V_{d1} = R_s i_{d1} + \frac{d\psi_{d1}}{dt} - \omega_e \psi_{q1} \\ V_{q1} = R_s i_{q1} + \frac{d\psi_{q1}}{dt} + \omega_e \psi_{d1} \\ \psi_{d1} = L_d i_{d1} + \psi_m \\ \psi_{q1} = L_q i_{q1}. \end{cases} \tag{1}$$

The *d3-q3* stator voltage vector components $V_{d3}$, $V_{q3}$ and the *d3-q3* stator flux vector components $\psi_{d3}$, $\psi_{q3}$ are given by

$$\begin{cases} V_{d3} = R_s i_{d3} + \frac{d\psi_{d3}}{dt} - 3\omega_e \psi_{q3} \\ V_{q3} = R_s i_{q3} + \frac{d\psi_{q3}}{dt} + 3\omega_e \psi_{d3} \\ \psi_{d3} = L_{sl} i_{d3} \\ \psi_{q3} = L_{sl} i_{q3} \end{cases} \tag{2}$$

where $R_s$ is the stator resistance, $L_{sl}$ is the stator leakage inductance, $\psi_m$ is the PM flux linkage, $\omega_e$ is the rotor electrical speed, and $i_{d1}, i_{q1}, i_{d3}$, and $i_{q3}$ are the stator $d_1$-$q_1$ axes and $d_3$-$q_3$ axes currents, respectively. $L_d$ and $L_q$ are the stator *dq*-axes inductances. The state-space model of the five-phase PMSM can be described as follows:

$$\begin{cases} \frac{di_{d1}}{dt} = -\frac{R_s}{L} i_{d1} + \omega_e i_{q1} + \frac{V_{d1}}{L} \\ \frac{di_{q1}}{dt} = -\frac{R_s}{L} i_{q1} - \omega_e i_{d1} + \frac{V_{q1}}{L} - \frac{\psi_m}{L}\omega_e \\ \frac{di_{d3}}{dt} = -\frac{R_s}{L_{sl}} i_{d3} + 3\omega_e i_{q3} + \frac{V_{d3}}{L_{sl}} \\ \frac{di_{q3}}{dt} = -\frac{R_s}{L_{sl}} i_{q3} - 3\omega_e i_{d3} + \frac{V_{q3}}{L_{sl}}. \end{cases} \tag{3}$$

The mechanical dynamic equations of the five-phase PMSM can be described as follows:

$$\begin{cases} \frac{d\omega_e}{dt} = -\frac{B}{J}\omega_e + \frac{p}{J}(T_e - T_l) \\ \frac{d\theta_e}{dt} = \omega_e \end{cases} \tag{4}$$

where $\theta_e$ is the rotor electrical position, *B* is the friction coefficient, *J* is the moment of inertia, *p* is the number of pole pairs, $T_l$ is the load torque, and $T_e$ is the developed torque. The developed torque in PMSM is the resultant of two components; namely the electromagnetic torque $(T_{\rm em})$ and the reluctance torque $(T_{\rm rel})$ as described as follows:

$$T_e = T_{\rm em} + T_{\rm rel} = \frac{5}{2} p\, \psi_m i_q + \frac{5}{2} p\, (L_d - L_q)\, i_d i_q. \tag{5}$$

In this article, the control of surface mounted PMSM (SPMSM) is studied, which has negligible reluctance torque $(L_d = L_q = L)$. Therefore, the torque equation is modified as follows:

$$T_e = T_{\rm em} = \frac{5}{2} p\, \psi_m i_q. \tag{6}$$

## III. Conventional MPC Methods

### A. Conventional FCS-MPC Techniques

According to the state-space model of the PMSM, the *dq*-axes currents in the next step can be predicted from the measured values using Euler approximation as follows:

$$\begin{cases} {i_{d1}}^{k+1} = \left(1 - \frac{R_s}{L} T_s\right) {i_{d1}}^k + T_s\, {\omega_e}^k\, {i_{q1}}^k + \frac{T_s}{L} {V_{d1}}^k \\ {i_{q1}}^{k+1} = \left(1 - \frac{R_s}{L} T_s\right) {i_{q1}}^k - T_s\, {\omega_e}^k\, {i_{d1}}^k + \frac{T_s}{L} {V_{q1}}^k \\ \qquad\qquad - \frac{\psi_m}{L} T_s\, {\omega_e}^k \\ {i_{d3}}^{k+1} = \left(1 - \frac{R_s}{L_{sl}} T_s\right) {i_{d3}}^k + 3\, T_s\, {\omega_e}^k\, {i_{q3}}^k + \frac{T_s}{L_{sl}} {V_{d3}}^k \\ {i_{q3}}^{k+1} = \left(1 - \frac{R_s}{L_{sl}} T_s\right) {i_{q3}}^k - 3\, T_s\, {\omega_e}^k\, {i_{d3}}^k + \frac{T_s}{L_{sl}} {V_{q3}}^k \end{cases} \tag{7}$$

where $T_s$ is the sampling interval. In the conventional MPC algorithms, the predicted stator currents, corresponding to the available switching states, are compared with their reference values to select the optimal state. The optimal switching state is applied in the next sampling interval. The *d1-q1-d3-q3-zero* voltage vectors matrix, $[\,{V_{d1}}^k\ {V_{q1}}^k\ {V_{d3}}^k\ {V_{q3}}^k\ {V_0}^k\,]^T$, can be calculated from axes transformation of the output phase voltages of the five-phase inverter as follows:

$$\begin{bmatrix} {V_{d1}}^k \\ {V_{q1}}^k \\ {V_{d3}}^k \\ {V_{q3}}^k \\ {V_0}^k \end{bmatrix} = \frac{1}{5} V_{\rm dc} \boldsymbol{\Gamma_c} \begin{bmatrix} 4 & -1 & -1 & -1 & -1 \\ -1 & 4 & -1 & -1 & -1 \\ -1 & -1 & 4 & -1 & -1 \\ -1 & -1 & -1 & 4 & -1 \\ -1 & -1 & -1 & -1 & 4 \end{bmatrix} \times \begin{bmatrix} {S_a}^k \\ {S_b}^k \\ {S_c}^k \\ {S_d}^k \\ {S_e}^k \end{bmatrix} \tag{8}$$

where ${S_x}^k$ is the switching function of phase $x (x \in \{a, b, c, d, e\})$. $\boldsymbol{\Gamma_c}$ is the coordinate transformation matrix, which transfer the five-phases (*a-b-c-d-e*) coordinates to (*d1-q1-d3-q3-zero*) coordinates, and it can be formulated as follows:

$$\boldsymbol{\Gamma_c} = \boldsymbol{C_{s/r}} \times \boldsymbol{\Gamma} = \begin{bmatrix} \cos(\theta_e) & \sin(\theta_e) & 0 & 0 & 0 \\ -\sin(\theta_e) & \cos(\theta_e) & 0 & 0 & 0 \\ 0 & 0 & 1 & 0 & 0 \\ 0 & 0 & 0 & 1 & 0 \\ 0 & 0 & 0 & 0 & 1 \end{bmatrix} \times \frac{2}{5} \begin{bmatrix} 1 & \cos(\alpha) & \cos(2\alpha) & \cos(3\alpha) & \cos(4\alpha) \\ 0 & \sin(\alpha) & \sin(2\alpha) & \sin(3\alpha) & \sin(4\alpha) \\ 1 & \cos(3\alpha) & \cos(6\alpha) & \cos(9\alpha) & \cos(12\alpha) \\ 0 & \sin(3\alpha) & \sin(6\alpha) & \sin(9\alpha) & \sin(12\alpha) \\ 0.5 & 0.5 & 0.5 & 0.5 & 0.5 \end{bmatrix} \tag{9}$$

where $\alpha = \frac{2\pi}{5}$. This matrix consists of two conversion matrices; The matrix $\boldsymbol{C_{s/r}}$ transforms the sine winding five-phase PMSM model in the ($\alpha 1$-$\beta 1$-$\alpha 3$-$\beta 3$-*zero*) stationary coordinates to (*d1-q1-d3-q3-zero*) synchronous rotating coordinates, while the matrix $\boldsymbol{\Gamma}$ transforms from (*a-b-c-d-e*) coordinates to ($\alpha 1$-$\beta 1$-$\alpha 3$-$\beta 3$-*zero*) coordinates.

It is well known that the conventional FCS-MPC performs large number of calculations during every sampling interval, which may delay the applied switching state to the next sampling interval. Therefore, a compensation for this delay is important so that the controller does not loss the reference tracking. The compensation is done by calculating the stator currents at ($k$+2)th sampling instant from the predicted ($k$+1)th values by modifying (7), assuming constant speed during one sampling

interval.

$$\begin{cases} {i_{d1}}^{k+2} = \left(1 - \frac{R_s}{L} T_s\right) {i_{d1}}^{k+1} + T_s {\omega_e}^k \, {i_{q1}}^{k+1} + \frac{{V_{d1}}^{k+1}}{L} T_s \\ {i_{q1}}^{k+2} = \left(1 - \frac{R_s}{L} T_s\right) {i_{q1}}^{k+1} - T_s {\omega_e}^k \, {i_{d1}}^{k+1} \\ \qquad + \frac{{V_{q1}}^{k+1}}{L} T_s - \frac{\psi_m}{L} \, T_s \, {\omega_e}^k \\ {i_{d3}}^{k+2} = \left(1 - \frac{R_s}{L_{sl}} T_s\right) {i_{d3}}^{k+1} + 3 T_s {\omega_e}^k \, {i_{q3}}^{k+1} + \frac{{V_{d3}}^{k+1}}{L_{sl}} T_s \\ {i_{q3}}^{k+2} = \left(1 - \frac{R_s}{L_{sl}} T_s\right) {i_{q3}}^{k+1} - 3 T_s {\omega_e}^k \, {i_{d3}}^{k+1} + \frac{{V_{q3}}^{k+1}}{L_{sl}} T_s. \end{cases} \tag{10}$$

There are three types of conventional FCS-MPC, which are applied on this system namely; FCS-MPC11 [40], which uses the zero-vector and 10 active vectors (blue trajectory in Fig. 2), FCS-MPC21 [41], which uses the zero vectors in addition to 20 active vectors (blue + green trajectory in Fig. 2), in addition to FCS-MPC31, which uses all the available real voltage vectors. The difference between these methods is the number of available switching states and voltage vectors. Larger number of voltage vectors gives higher degree of freedom to the controller to select the best voltage vector. However, greater number of voltage vectors means increased number of calculation processes during the sampling interval and increased computational burden on the controller.

In these methods the optimal voltage vector is selected according to a predefined cost function. The cost function, in this case, is formulated in order to minimize the error between the reference and the predicted currents at the ($k$+2)th sampling interval, as follows:

$$G_i = \left| {i_{d1}^*}^{k+2} - {i_{d1}}^{k+2} \right|^2 + \left| {i_{q1}^*}^{k+2} - {i_{q1}}^{k+2} \right|^2 + \left| {i_{d3}^*}^{k+2} - {i_{d3}}^{k+2} \right|^2 + \left| {i_{q3}^*}^{k+2} - {i_{q3}}^{k+2} \right|^2 \tag{11}$$

where the superscription $(*)$ represents the reference value.

### B. FCS-MPCC With Virtual Voltage Vectors (FCS-MPCC-V3).

It has been noticed in [24], that the aligned large (blue) and medium (green) voltage vectors are in opposite directions on the $\alpha_3$-$\beta_3$ plane, and they have different amplitudes. Hence, the $d_3$-$q_3$ voltage and current components (third harmonics) can be minimized by modulating the aligned large and medium voltage vectors and adapting their amplitudes. The adaption of the amplitudes of these vectors can be done by the modulation of the aligned large and medium vectors with optimal dwell times during each sampling interval. It has been found that the optimal dwell times for the large and medium vectors are 0.618 and 0.382, respectively, and the standard way to modulate both vectors is illustrated in Fig. 3(a).

The resulting voltage vectors are ten optimal V3, as shown in the $\alpha_1$-$\beta_1$ and $\alpha_3$-$\beta_3$ planes of Fig. 3(b). It is clear that the resultant V3 have minimized third harmonic component. FCS-MPCC-V3 presents better performance than the conventional FCS-MPC with reduced number of calculations during each sampling interval, since there are only 11 vectors (11 feasible vectors in the optimization process).

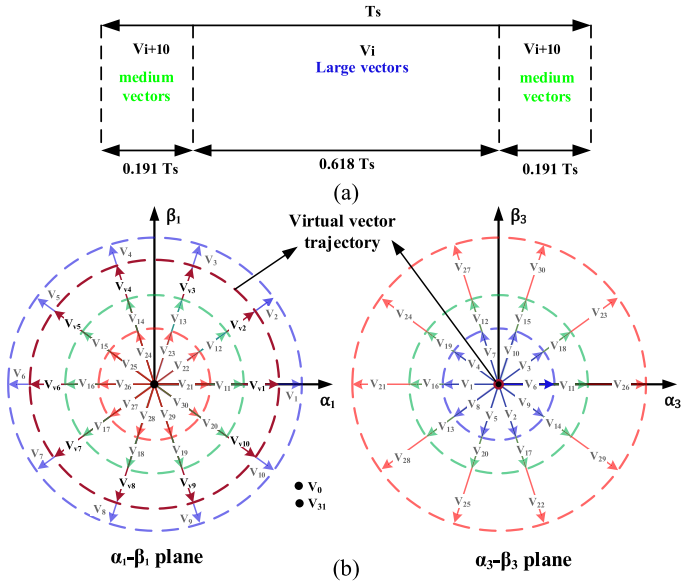


Fig. 3. Optimal V3 generation in five-phase 2L-VSI. (a) Modulation technique. (b) Resultant V3 trajectory.

For further performance improvement, an enhanced FCS-MPC considering a duty ratio optimization (FCS-MPCC-V3-DRO) has been applied on VSI with RL load in [26]. This algorithm optimizes the time duration of the optimal V3 in order to minimize the error between the reference and the predicted fundamental currents using (12), as shown at the bottom of this page. This optimization results in significant reduction in the current harmonics and the torque ripples, however, the calculation of the optimal time duration $(t_{\text{opt}})$ adds more complexity to the algorithm.

All the previous FCS-MPC methods incur high computational burden because they involve the exploration process for all the available voltage vectors in the control set. Therefore, the computational burden still needs to be reduced.

### C. Low-Complexity Hysteresis MPTC

The basic principle of this method is the same as the conventional FCS-MPTC, which uses the electromagnetic torque and the stator flux as the control variables. Only two vectors are selected from the control-set to be tested every control interval. Furthermore, the cost function is significantly simplified to include only two parts without weighting factors.

$$t_{\text{opt}j} = \frac{\left[ {V_{vj\alpha}}^{k+2} \, i_{\alpha 1}^* + {V_{vj\beta}}^{k+2} \, i_{\beta 1}^* \right] (R_s T_s + L) - L \left[ {V_{vj\alpha}}^{k+2} \, {i_{\alpha 1}}^{k+1} + {V_{vj\beta}}^{k+2} \, {i_{\beta 1}}^{k+1} \right]}{\left[ \left( {V_{vj\alpha}}^{k+2} \right)^2 + \left( {V_{vj\beta}}^{k+2} \right)^2 \right]} \tag{12}$$

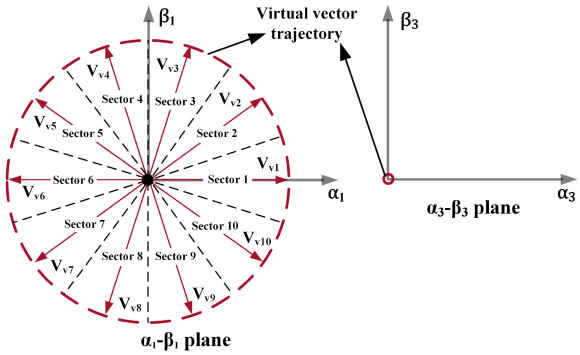


Fig. 4. Sector definition of the virtual vectors in the complex plane.

TABLE I
BEST VOLTAGE VECTORS LOOKUP TABLE FOR HYSTERESIS MPTC

| $H_f$ | $H_{Te}$ | Sector Number 1 | 2 | 3 | 4 | 5 | 6 | 7 | 8 | 9 | 10 |
|---|---|---|---|---|---|---|---|---|---|---|---|
| 1 | 1 | $V_{v2}$ $V_{v3}$ | $V_{v3}$ $V_{v4}$ | $V_{v4}$ $V_{v5}$ | $V_{v5}$ $V_{v6}$ | $V_{v6}$ $V_{v7}$ | $V_{v7}$ $V_{v8}$ | $V_{v8}$ $V_{v9}$ | $V_{v9}$ $V_{v10}$ | $V_{v10}$ $V_{v1}$ | $V_{v1}$ $V_{v2}$ |
| | -1 | $V_{v9}$ $V_{v10}$ | $V_{v10}$ $V_{v1}$ | $V_{v1}$ $V_{v2}$ | $V_{v2}$ $V_{v3}$ | $V_{v3}$ $V_{v4}$ | $V_{v4}$ $V_{v5}$ | $V_{v5}$ $V_{v6}$ | $V_{v6}$ $V_{v7}$ | $V_{v7}$ $V_{v8}$ | $V_{v8}$ $V_{v9}$ |
| -1 | 1 | $V_{v4}$ $V_{v5}$ | $V_{v5}$ $V_{v6}$ | $V_{v6}$ $V_{v7}$ | $V_{v7}$ $V_{v8}$ | $V_{v8}$ $V_{v9}$ | $V_{v9}$ $V_{v10}$ | $V_{v10}$ $V_{v1}$ | $V_{v1}$ $V_{v2}$ | $V_{v2}$ $V_{v3}$ | $V_{v3}$ $V_{v4}$ |
| | -1 | $V_{v7}$ $V_{v8}$ | $V_{v8}$ $V_{v9}$ | $V_{v9}$ $V_{v10}$ | $V_{v10}$ $V_{v1}$ | $V_{v1}$ $V_{v2}$ | $V_{v2}$ $V_{v3}$ | $V_{v3}$ $V_{v4}$ | $V_{v4}$ $V_{v5}$ | $V_{v5}$ $V_{v6}$ | $V_{v6}$ $V_{v7}$ |

The general procedure of this method is summarized with the following steps [39].

*Step 1:* The torque and the stator flux linkage are estimated, considering one step delay compensation, using the following equations:

$$T_e{}^{k+1} = \frac{5}{2} p\, \psi_{\rm m}\, i_{q1}{}^{k+1} \tag{13}$$

$$\begin{cases} \psi_{s1}{}^{k+1} = \sqrt{\left[L\, i_{d1}{}^{k+1} + \psi_{\rm m}\right]^2 + \left[L\, i_{q1}{}^{k+1}\right]^2} \\ \psi_{s3}{}^{k+1} = \sqrt{\left[L_{ls} i_{d3}{}^{k+1}\right]^2 + \left[L_{ls} i_{q3}{}^{k+1}\right]^2}. \end{cases} \tag{14}$$

*Step 2:* Two hysteresis comparators are used to indicate the required trends on the electromagnetic torque and the stator flux to track their reference values. The outputs of the hysteresis controllers $(H_{Te}, H_{\psi})$ are described as follows:

$$H_{Te} = \begin{cases} +1 & T_e < T_e^* \\ -1 & T_e > T_e^* \end{cases} \tag{15}$$

$$H_{\psi} = \begin{cases} +1 & \psi_{s1} < \psi_{s1}^* \\ -1 & \psi_{s1} > \psi_{s1}^* \end{cases} \tag{16}$$

where $T_e^*$ and $\psi_{s1}^*$ are the reference electromagnetic torque and the fundamental reference stator flux, respectively.

*Step 3:* The outputs of the hysteresis comparators are used to select the suitable voltage vectors, which result in the required trends of the electromagnetic torque and the stator flux. According to these trends, the control plane of the fundamental stator flux linkage is divided into ten sectors, the same as in Fig. 4. From the analysis discussed in [39], only two virtual vectors produce similar effects on the torque and the stator flux trends, as listed in the lookup Table I. These two vectors are defined from the outputs of the hysteresis comparators and the sector number.

The sector number is defined from the angle of the fundamental stator flux vector as follows:

$$S_n = \text{floor}\left(\frac{\angle \psi_{s1}{}^{k+1} + \pi/10}{\pi/5}\right) + 1. \tag{17}$$

*Step 4:* For the selected two vectors, the optimal duration time is calculated in order to minimize the error between the predicted and the reference torques at the $(k+2)$th instant

$$\begin{aligned} &T_e^* - T_e{}^{k+2} \\ &= T_e^* - \left(T_e{}^k + \delta_{Tvir} t_{\rm opt} + \delta_{T0}\left(T_s - t_{\rm opt}\right)\right) \to \text{zero} \end{aligned} \tag{18}$$

where $\delta_{Tvir}$, $\delta_{T0}$ are the torque variations due to applying the virtual vector and the zero-vector, respectively. The effect of the stator voltage on the electromagnetic torque can be described as follows:

$$\delta_T = \frac{dT_e}{dt} = \frac{5p\psi_{\rm m}}{2L_q}\left(V_{q1} - R_s i_{q1} - L_d \omega_e i_{d1} - \psi_m \omega_e\right). \tag{19}$$

If (18) is reformulated, the optimal time duration for the virtual vector can be calculated using the following formula:

$$t_{\rm opt} = \frac{T_e^* - T_e{}^k - \delta_{T0} T_s}{\delta_{Tvir} - \delta_{T0}}. \tag{20}$$

*Step 5:* The optimal V3 is selected to be applied in the next sampling interval from the best two vectors according to the following simplified cost function:

$$G_i = \left|\psi_{s1}{}^{k+2} - \psi_{s1}^*\right|^2 + F_m \tag{21}$$

where the fundamental flux linkage $(\psi_{s1}{}^{k+2})$ is predicted at the $(k+2)$th sampling interval as follows:

$$\psi_{s1}{}^{k+2} = \sqrt{\left[L\, i_{d1}{}^{k+2} + \psi_{\rm m}\right]^2 + \left[L\, i_{q1}{}^{k+2}\right]^2}. \tag{22}$$

$F_m$ is the overcurrent protection cost function, which is given as follows:

$$F_m = \begin{cases} \inf & if\ |i_s| > i_{\max} \\ \text{zero} & if\ |i_s| \le i_{\max}. \end{cases} \tag{23}$$

where $|i_s| = \sqrt{i_{d1}{}^2 + i_{q1}{}^2}$.

The block diagram of the hysteresis MPTC strategy is shown in Fig. 5. It is clear that this algorithm has low complexity because its exploration process is reduced to include only two vectors. However, the proposed algorithm minimizes the computational burden by cancelling the exploration process, as explained in the following section.

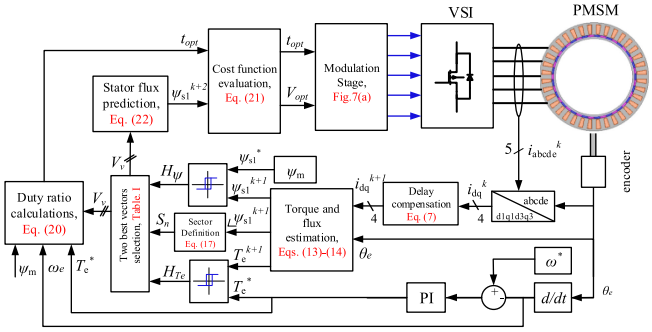


Fig. 5. Block diagram of the low-complexity hysteresis MPTC.

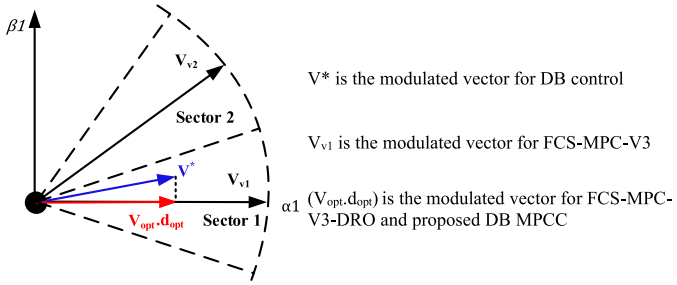


Fig. 6. Vector representation of the optimal voltage vector for DB and MPC controllers.

## IV. Proposed DB MPCC

### A. Reference Voltage Calculation

There are two different conventional methods for direct reference voltage calculation. The first method is based on PI current controller with carrier-based pulsewidth modulation (PI-CBPWM). This method has the advantage of less sensitivity to the model parameters and improved steady-state parameters. However, it suffers from slightly higher computational burden and difficult tuning of the controller parameters. In addition, the dynamic response of the PI controller is generally slow [11]. The second calculation method is based on the DB principles, which is much simpler and considers the system nonlinearity. Therefore, the proposed algorithm estimates the reference voltage vector using the DB control principles. Like the previous MPC algorithm, one-step digital delay compensation is considered in this method, as given in (7). From (10), the ($d1$-$q1$-$d3$-$q3$) voltages are given as follows:

$$\begin{cases} {V_{d1}}^{k+1} = L\frac{{i_{d1}}^{k+2}-{i_{d1}}^{k+1}}{T_s} + {i_{d1}}^{k+1}R_s - {\omega_e}^k{i_{q1}}^{k+1}L \\ {V_{q1}}^{k+1} = L\frac{{i_{q1}}^{k+2}-{i_{q1}}^{k+1}}{T_s} + {i_{q1}}^{k+1}R_s \\ \qquad + {\omega_e}^k{i_{d1}}^{k+1}L + \psi_m{\omega_e}^k \\ {V_{d3}}^{k+1} = L_{ls}\frac{{i_{d3}}^{k+2}-{i_{d3}}^{k+1}}{T_s} + {i_{d3}}^{k+1}R_s - 3{\omega_e}^k{i_{q3}}^{k+1}L_{ls} \\ {V_{q3}}^{k+1} = L_{ls}\frac{{i_{q3}}^{k+2}-{i_{q3}}^{k+1}}{T_s} + {i_{q3}}^{k+1}R_s + 3{\omega_e}^k{i_{d3}}^{k+1}L_{ls}. \end{cases} \tag{24}$$

If the predicted currents at the ($k$+2)th instant is replaced with reference currents, the reference voltages are given as follows:

$$\begin{cases} V_{d1}^* = L\frac{i_{d1}^*-{i_{d1}}^{k+1}}{T_s} + {i_{d1}}^{k+1}R_s - {\omega_e}^k{i_{q1}}^{k+1}L \\ V_{q1}^* = L\frac{i_{q1}^*-{i_{q1}}^{k+1}}{T_s} + {i_{q1}}^{k+1}R_s + {\omega_e}^k{i_{d1}}^{k+1}L + \psi_m{\omega_e}^k \\ V_{d3}^* = L_{ls}\frac{i_{d3}^*-{i_{d3}}^{k+1}}{T_s} + {i_{d3}}^{k+1}R_s - 3{\omega_e}^k{i_{q3}}^{k+1}L_{ls} \\ V_{q3}^* = L_{ls}\frac{i_{q3}^*-{i_{q3}}^{k+1}}{T_s} + {i_{q3}}^{k+1}R_s + 3{\omega_e}^k{i_{d3}}^{k+1}L_{ls}. \end{cases} \tag{25}$$

The reference voltage vectors can be calculated by coordinates conversion from the rotating coordinates ($d_1$-$q_1$-$d_3$-$q_3$-zero) $V_{d1q1d3q30}$ to stationary coordinates ($\alpha1$-$\beta1$-$\alpha3$-$\beta3$-*zero*) $V_{\alpha1\beta1\alpha3\beta30}$ as follows:

$$V_{\alpha1\beta1\alpha3\beta30} = C_{s/r}^{-1} \times V_{d1q1d3q30} \tag{26}$$

$$\begin{cases} V_1^* = V_{\alpha1}^* + jV_{\beta1}^* \\ V_3^* = V_{\alpha3}^* + jV_{\beta3}^*. \end{cases} \tag{27}$$

### B. Optimal Voltage Vector Selection

The difference between the conventional DB controller and MPC is the modulated voltage vector, as shown in Fig. 6. The conventional DB controller uses the calculated reference voltage vector, regardless of the switching effort, to eliminate the tracking error in the next sampling interval. On the other hand, MPC algorithms select the best approximation for the reference voltage vector from the available control set according to the required constraints [42]. FCS-MPC without constraints is considered as a quantized DB control. Compared with MPC, the DB controller exhibits low complexity and improved the steady-state performance. However, the FCS-MPC shows faster dynamic response and less sensitivity to parameters mismatches and measurements noise [43], [44].

The proposed algorithm is a combination between the DB controller and MPC. While the reference voltage vector calculation is done based on the DB principles, the modulated voltage vector is the same vector that selected by the FCS-MPC from the control set. The control set, in this case, is the ten enhanced V3 in order to eliminate the third harmonic components. The selected voltage vector should represent the best approximation of the reference voltage. Since the amplitudes of all ten V3 in the $\alpha_3$-$\beta_3$ plane are approximately zero, all vectors exhibit the same effect in the $\alpha_3$-$\beta_3$ plane. Thus, the optimal voltage vector is selected according to the fundamental reference voltage $V_1^*$.

The $\alpha_1$-$\beta_1$ plane is divided into ten sectors; each sector contains one optimal voltage vector, as indicated in Fig. 4. The selection of the optimal voltage vector depends on the location of the fundamental reference voltage vector $V_1^*$. The sector number of the fundamental reference voltage can be defined using the angle of the fundamental reference voltage vector, as shown in the following:

$$S_n = \text{floor}\left(\frac{\angle V_1^* + \pi/10}{\pi/5}\right) + 1. \tag{28}$$

### C. Optimal Duration Time Calculation

Equation (28) defines the reference voltage sector from 1 to 10. The selected optimal V3 is applied for the optimal duration

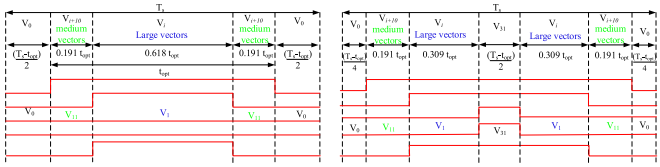


Fig. 7. Modulation processes. (a) Reduced switching frequency modulation. (b) Constant switching frequency modulation.

time, and the zero-vector is applied for the remaining part of the sampling interval. The optimal duration time is calculated in order to minimize the error between the reference voltage vectors $(V_1^*, V_3^*)$ and the selected optimal voltage vectors $(V_{1\text{opt}}, V_{3\text{opt}})$ as follows:

$$t_{\text{opt}} = \min_{t_{\text{opt}}} G \tag{29}$$

$$G = \left(V_1^* - V_{1\text{opt}} \frac{t_{\text{opt}}}{T_s}\right)^2 + \left(V_3^* - V_{3\text{opt}} \frac{t_{\text{opt}}}{T_s}\right)^2. \tag{30}$$

The cost function $G$, in this case, represents the error between the reference voltage vector and the selected optimal voltage vector. To calculate $t_{\text{opt}}$ that minimizes $G$, the first derivative of $G$ with respect to $t_{\text{opt}}$ should equal zero. This yields to the following expression of $t_{\text{opt}}$:

$$t_{\text{opt}} = \frac{(V_1^* \odot V_{1\text{opt}}) + (V_3^* \odot V_{3\text{opt}})}{|V_{1\text{opt}}|^2 + |V_{3\text{opt}}|^2} \times T_s \tag{31}$$

where $\odot$ means the dot product operator of the two vectors. The optimal time duration $t_{\text{opt}}$ should be limited within the range $0 \le t_{\text{opt}} \le T_s$.

### *D. Enhanced Pulse-width Modulation (EPWM)*

The modulation of the selected optimal voltage vector with the duty ratio should be symmetrical to the central point of the sampling interval, as shown in Fig. 7. There are two types of modulation techniques available in this case. The first one produces a reduced switching frequency by using one zero-voltage vector $(V_0)$ during every control interval, as indicated in Fig. 7(a). Although this modulation technique produces reduced switching frequency, the average switching frequency of this modulation is almost constant [39]. The duty cycles of the converter switches are calculated from the selected optimal voltage vector and the optimal duration time, as shown in the following:

$$\begin{bmatrix} d_a \\ d_b \\ d_c \\ d_d \\ d_e \end{bmatrix} = \left( 0.618 \times \begin{bmatrix} S_a \\ S_b \\ S_c \\ S_d \\ S_e \end{bmatrix}_{\text{opt}|l} + 0.382 \times \begin{bmatrix} S_a \\ S_b \\ S_c \\ S_d \\ S_e \end{bmatrix}_{\text{opt}|m} \right) \times \frac{t_{\text{opt}}}{T_s} \tag{32}$$

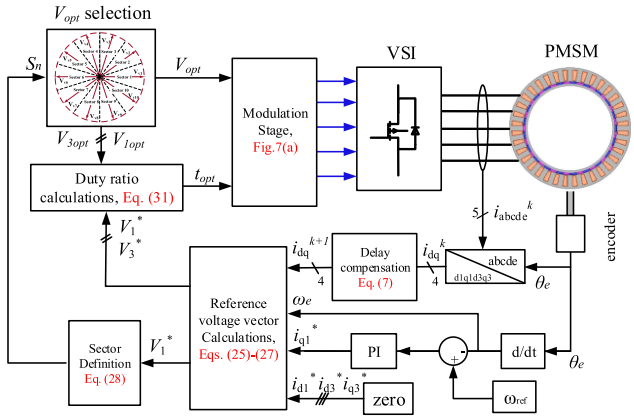


Fig. 8. Block diagram of the proposed MPC technique.

where the subscriptions $\text{opt}|l$ and $\text{opt}|m$ represent the large and the medium vectors, respectively, which result in the selected optimal V3. The second modulation technique assures constant switching frequency operation by adopting the two zero vectors $V_0$ and $V_{31}$ with symmetrical PWM, as indicated in Fig. 7(b). This modulation technique is typically similar to the conventional SVPWM. In this case, the duty cycles of the converter can be formulated as follows:

$$\begin{bmatrix} d_a \\ d_b \\ d_c \\ d_d \\ d_e \end{bmatrix} = \left( 0.618 \times \begin{bmatrix} S_a \\ S_b \\ S_c \\ S_d \\ S_e \end{bmatrix}_{\text{opt}|l} + 0.382 \times \begin{bmatrix} S_a \\ S_b \\ S_c \\ S_d \\ S_e \end{bmatrix}_{\text{opt}|m} \right) \times \frac{t_{\text{opt}}}{T_s} + \frac{T_s - t_{\text{opt}}}{2T_s}. \tag{33}$$

Both modulation techniques have the same effect on the average values of the controlled variables as the original PWM process. In this article, considering the high-power drive system, the reduced switching frequency modulation is applied.

The block diagram of the proposed DB MPCC technique is shown in Fig. 8. The proposed method has the advantage of reduced computational burden, since it does not require neither the enumeration process for testing all available voltage vectors as in the conventional MPC, nor testing two voltage vectors as the case of the hysteresis MPTC. In addition, there is no additional hysteresis controller in the proposed DB MPCC controller. These advantages reduce the execution time of the proposed technique. Therefore, the hardware implementation of the proposed algorithm becomes easier and possible using a standard low-cost digital controller.

The flowcharts of the proposed DB MPCC and the hysteresis MPTC are compared in Fig. 9. The required arithmetic processes of the studied algorithms are compared in Table II. It is clear from Table II that the required number of mathematical operations in

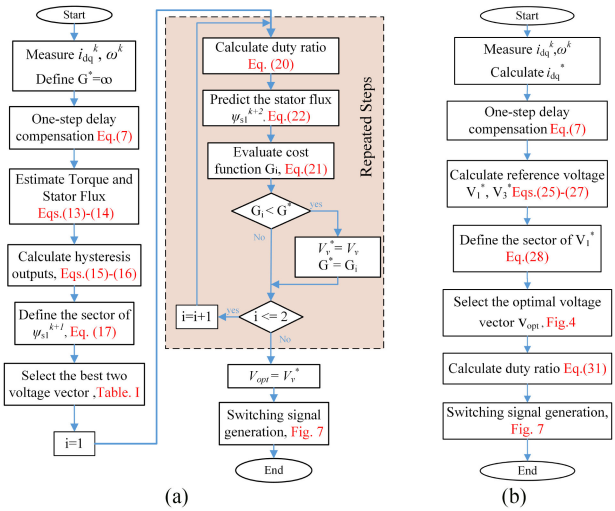


Fig. 9. Flowcharts of (a) Hysteresis MPTC, and (b) Proposed DB MPCC.

TABLE II
COMPARISON OF ARITHMETIC OPERATIONS COUNT BETWEEN THE STUDIED ALGORITHMS

| | Multiplications | Additions | Subtractions | Divisions | Total Operations |
|---|---|---|---|---|---|
| **FCS-MPCC31** | 1104 | 388 | 388 | 295 | 2175 |
| **FCS-MPCC21** | 764 | 268 | 268 | 205 | 1505 |
| **FCS-MPCC11** | 424 | 148 | 148 | 115 | 835 |
| **FCS-MPCC-V3** | 439 | 153 | 153 | 115 | 860 |
| **FCS-MPCC-V3-DRO** | 449 | 157 | 154 | 116 | 876 |
| **Hysteresis-MPTC** | 158 | 81 | 25 | 17 | 281 |
| **DB MPCC** | 35 | 25 | 12 | 10 | 82 |

the proposed DB MPCC is the lowest among all existing MPC algorithms.

## V. SIMULATION RESULTS

To verify the potentials of the proposed DB MPCC algorithm, a Simulink model for a five-phase PMSM drive system with the DB MPCC control technique is implemented. Furthermore, the proposed control technique is compared with three existing MPC techniques applied on five-phase PMSM drives; namely FCS-MPCC-V3, FCS-MPCC-V3-DRO, and hysteresis MPTC with the same system parameters. The system parameters are listed in Table III. The speed loop PI controller gains are designed as explained in [45] and [46].

### A. Steady-State Performance

The steady-state performance of the proposed DB MPCC technique is investigated and compared with the other studied algorithms at 80 rad/s and load torque of 15 N·m, as shown in Fig. 10. The sampling time is set as 200 $\mu$s to obtain low switching frequency for high-power applications. The results show that FCS-MPCC-V3 algorithm has the highest harmonics and ripples compared with other methods due to the absence of duty ratio optimization.

TABLE III
IMPLEMENTED SYSTEM PARAMETERS FOR SIMULATION

| Machine Type | SPMSM |
|---|---|
| Number of phases | 5 |
| DC-link voltage ($V_{dc}$) | 110 V |
| Maximum current ($I_{max}$) | 10 A |
| d-axis inductance ($L_d$) | 8.5 mH |
| q-axis inductance ($L_q$) | 8.5 mH |
| Stator resistance ($R_s$) | 1.875 Ω |
| PM flux linkage ($\psi_m$) | 0.2 Wb. |
| Pole pairs (p) | 4 |
| Moment of Inertia (J) | 0.008 Kg.m$^2$ |
| Speed loop PI controller gains | |
| $K_{p\_\omega}$ | 0.32 |
| $K_{i\_\omega}$ | 5.12 |

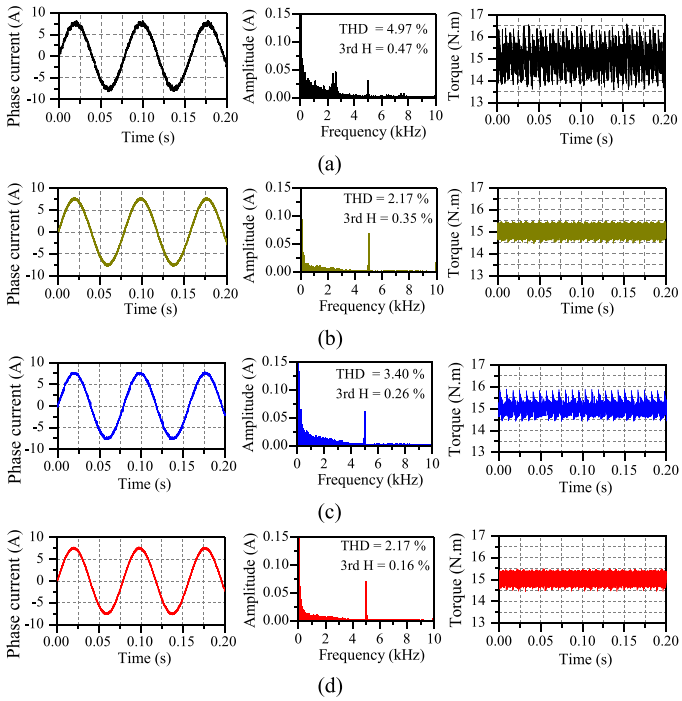


Fig. 10. Steady-state performance comparison of studied algorithms at rated condition. (a) FCS-MPCC-V3. (b) FCS-MPCC-V3-DRO. (c) Hysteresis MPTC. (d) Proposed DB MPCC.

The FFT analysis of the stator currents indicates that the proposed DB MPCC, is similar to the FCS-MPCC-V3-DRO, has lower total harmonic distortion (THD) compared with the hysteresis MPTC. Furthermore, the third-harmonic component of the DB MPCC is the lowest among all studied algorithms due to considering the third harmonic optimization in the duty-ratio calculation.

For further investigation and quantitative comparison, the steady-state torque ripples and the stator currents THD are compared for all studied methods at different rotor speeds, as depicted in Fig. 11. The torque ripples are calculated, for $n$ data points, using the following $l2-\text{norm}$ formula:

$$T_r = \sqrt{\frac{1}{n}\sum_{i=1}^{n}\left(T_{e\_i}^{*} - T_{e\_i}\right)^2}. \tag{34}$$

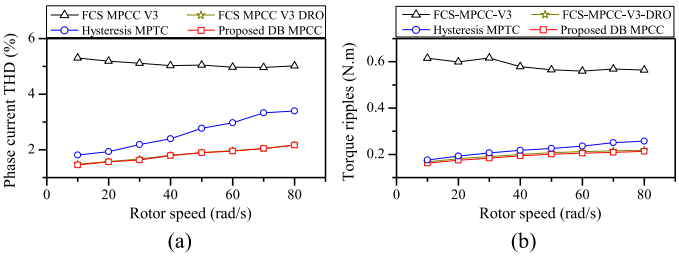


Fig. 11. Steady-state performance comparison of the studied control schemes at different rotor speeds. (a) Current THD curves. (b) Torque ripples curves.

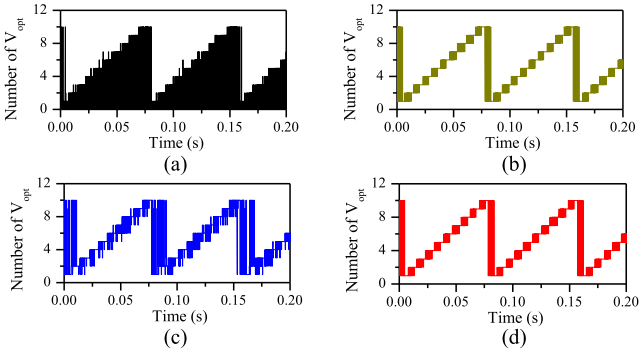


Fig. 12. A comparison of the selected optimal V3 from the studied control schemes. (a) FCS-MPCC-V3. (b) FCS-MPCC-V3-DRO. (c) Hysteresis MPTC. (d) Proposed DB MPCC.

Fig. 11 shows that the performance of the proposed DB MPCC at different rotor speeds is identical to that of the FCS-MPCC-V3-DRO. Both algorithms can achieve the lowest torque ripples and phase current THD at all rotor speeds compared with other studied methods. Both algorithms select the same optimal voltage vectors in different ways, as shown in Fig. 12. FCS-MPCC-V3-DRO selects the optimal vector using high computational enumeration process and cost function evaluation. In contrast, the DB solution of the proposed MPCC technique provides an explicit optimal voltage vector selection that makes the computational burden of the proposed algorithm much simpler. FCS-MPCC-V3 has the highest ripples and harmonics at all rotor speeds due to the absence of the duty ratio optimization. Therefore, this control scheme has to select one active vector in the present control interval and one zero vector in the next control interval, as indicated in Fig. 12. Hence, the FCS-MPCC-V3 results in much lower average switching frequency. The hysteresis MPTC method selects the optimal voltage vector from the two best vectors based on the cost function evaluation, which makes this selection stochastic to some extent. Hence, the hysteresis MPTC has a quite increased current harmonics and torque ripples.

The performances of the studied algorithms at different sampling intervals are quantitively compared in Table IV. This comparison proves the effectiveness of the proposed DB solution for optimal voltage vector selection, since it directly selects the same optimal voltage vector as the complex FCS-MPCC-V3-DRO. Furthermore, both control schemes have the best control performance compared with the hysteresis MPTC with the same

TABLE IV
COMPARISON AT DIFFERENT SAMPLING INTERVALS

| | FCS-MPCC-V3 | | | | FCS-MPCC-V3-DRO | | | | Hysteresis-MPTC | | | | Proposed DB MPCC | | | |
|---|---|---|---|---|---|---|---|---|---|---|---|---|---|---|---|---|
| $T_s(\mu s)$ | 100 | | 200 | | 100 | | 200 | | 100 | | 200 | | 100 | | 200 | |
| $\omega_e(rad/s)$ | 10 | 80 | 10 | 80 | 10 | 80 | 10 | 80 | 10 | 80 | 10 | 80 | 10 | 80 | 10 | 80 |
| $F_{sw}$(kHz) | 2.00 | 3.58 | 1.00 | 1.80 | 7.02 | 7.00 | 3.50 | 3.50 | 7.02 | 7.00 | 3.50 | 3.50 | 7.02 | 7.00 | 3.50 | 3.50 |
| THD (%) | 2.73 | 2.92 | 5.21 | 5.19 | 1.01 | 1.13 | 1.46 | 2.17 | 1.35 | 1.40 | 1.84 | 3.49 | 1.01 | 1.13 | 1.46 | 2.17 |
| $T_r(Nm)$ | 0.31 | 0.28 | 0.62 | 0.57 | 0.08 | 0.11 | 0.16 | 0.21 | 0.10 | 0.13 | 0.18 | 0.25 | 0.08 | 0.11 | 0.16 | 0.21 |

TABLE V
QUANTITIVELY COMPARISON UNDER SIMILAR AVERAGE SWITCHING FREQUENCY

| | $F_{sw}$(kHz) | $T_s(\mu s)$ | THD (%) | $T_r(Nm)$ |
|---|---|---|---|---|
| FCS-MPCC-V3 | 3.48 | 103 | 2.68 | 0.3024 |
| FCS-MPCC-V3-DRO | 3.5 | 200 | 2.17 | 0.21 |
| Hysteresis-MPTC | 3.5 | 200 | 3.49 | 0.25 |
| Proposed DB MPCC | 3.5 | 200 | 2.17 | 0.21 |

average switching frequency. This is because the transition between optimal vectors is similar in the three methods, as shown in Fig. 12. However, the hysteresis MPTC selection of the optimal vector is sometimes not accurate since it is dependent on the torque and flux cost functions optimization. As expected, the FCS-MPCC-V3 always has the lowest average switching frequency among the studied methods. The average switching frequency $(F_{\rm sw})$ is calculated as follows:

$$F_{\rm sw} = \frac{F_{{\rm ave},a} + F_{{\rm ave},b} + F_{{\rm ave},c} + F_{{\rm ave},d} + F_{{\rm ave},e}}{5} \tag{35}$$

where $F_{{\rm ave},a}, F_{{\rm ave},b}, F_{{\rm ave},c}, F_{{\rm ave},d}$, and $F_{{\rm ave},e}$ are the average switching frequencies of the five phases. It can be deduced from Table IV that the FCS-MPCC-V3 scheme has variable switching frequency with the rotor speed compared with other control schemes. In order to obtain fair comparison, the four control schemes are compared at the same average switching frequency in Table V. The proposed DB MPCC and the FCS-MPCC-V3-DRO schemes still have the advantage over the other two methods at the same average switching frequency.

### *B. Dynamic Performance*

To guarantee clear evaluation on the proposed technique, the four studied control schemes are compared under two dynamic cases; speed step change and load variations. Fig. 13 shows that the hysteresis MPTC technique has a little faster response than that of other studied techniques under speed step change condition. This is because the torque control techniques are faster than the current control schemes. The dynamic load torque response is tested by changing the load torque from 10 N·m to 15 N·m at 0.1 s, then the load torque is reduced again to 10 N·m again at 0.3 s. The response of all control methods under load torque variations are almost the same, as depicted in Fig. 14. The rotor speed is altered at the instant of the load torque step change, and it converges quickly to its reference value for all control schemes.

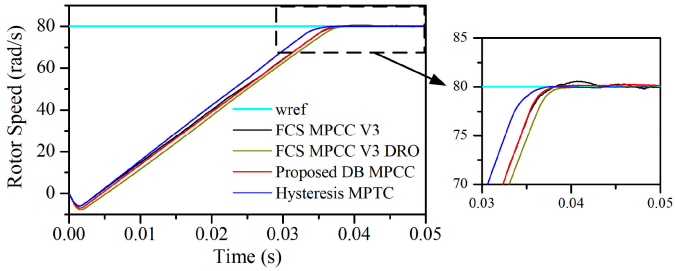


Fig. 13. Speed step change response.

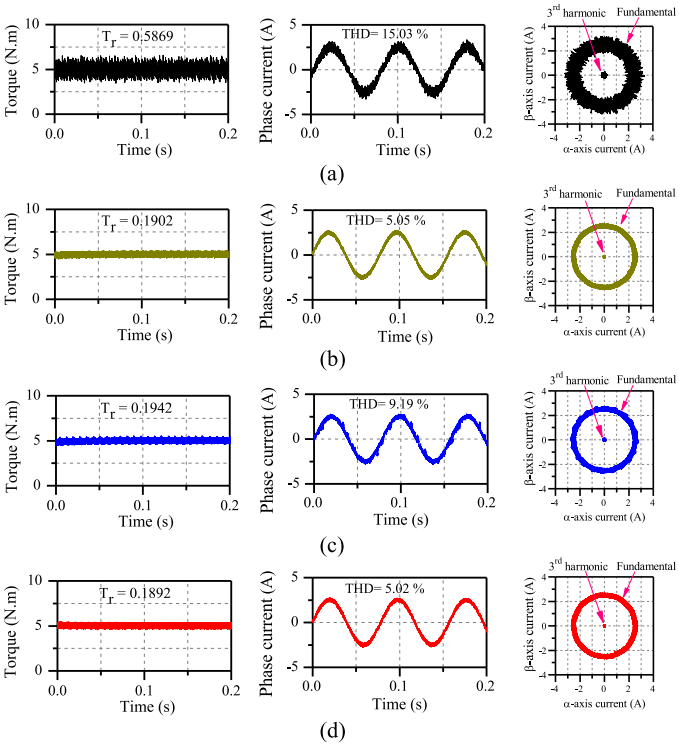


Fig. 14. Comparison of load change response (a) FCS-MPCC-V3. (b) FCS-MPCC-V3-DRO. (c) Hysteresis MPTC. (d) Proposed DB MPCC.

### C. Analysis and Comparison of Duty Ratio Calculations

One clear advantage of the proposed DB MPCC technique is that it has replaced the exploration process by the DB principles to select the optimal voltage vector. This way, the calculation processes are significantly reduced compared with previous techniques. In addition, the duty ratio optimization is calculated by minimizing the voltage error, which is considered more generalized way compared with the existing methods. For instance, the duty ratio optimization, which is proposed in [26], is dependent on the $\alpha_1$-$\beta_1$ stator currents error minimization, as indicated by (12). By substituting with the $\alpha_1$-$\beta_1$ voltage equations in (12), the optimal duty ratio $(d_{\text{opt}})$ can be calculated from $\alpha_1$-$\beta_1$ voltage error minimization as follows:

$$d_{\text{opt}} = \frac{\left(V_1^* \odot V_{1\text{opt}}\right)}{|V_{1\text{opt}}|^2}. \tag{36}$$

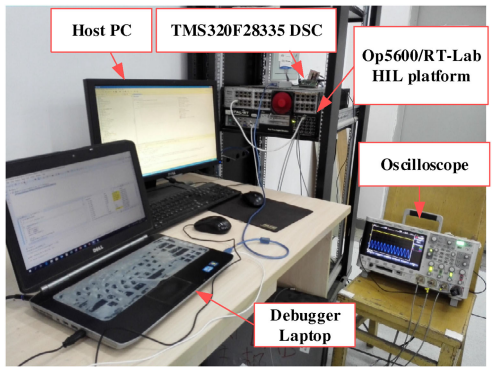


Fig. 15. Photo of HIL setup.

Another example is the duty ratio optimization, which is proposed by the hysteresis MPTC in [39]. In this method, the optimal duty ratio is based on the torque error minimization, as indicated by (20). By substituting with the torque and torque derivative equations, the duty ratio optimization is converted to $q$-axis voltage error minimization as follows:

$$d_{\text{opt}} = \frac{\left(V_{q1}^* \odot V_{q1\text{opt}}\right)}{|V_{q1\text{opt}}|^2}. \tag{37}$$

On the other hand, the proposed DB MPCC algorithm is considered more general because it takes into consideration the $\alpha_3$-$\beta_3$ voltage error in addition to the $\alpha_1$-$\beta_1$ voltage during the duty ratio optimization process. The optimal duty ratio of the DB MPCC can be given by converting (31) to per unit bases as follows:

$$d_{\text{opt}} = \frac{\left(V_1^* \odot V_{1\text{opt}}\right) + \left(V_3^* \odot V_{3\text{opt}}\right)}{|V_{1\text{opt}}|^2 + |V_{3\text{opt}}|^2}. \tag{38}$$

## VI. HIL Results

In order to validate the effectiveness of the proposed DB MPCC algorithm, a real-time HIL setup has been designed, as shown in Fig. 15. This platform uses a real-time RT-LAB OP5600 simulator for five-phase PMSM drive simulation, and TMS320F28335 digital signal processor (DSP) for algorithm implementation. The proposed DB MPCC as well as other studied control techniques have been implemented using the DSP. The system parameters are the same as the simulation parameters, which are listed in Table III, except the speed loop PI control gains. These parameters are redesigned with different cut-off frequency due to the measurement noise of the analog-to-digital converters. The new gains are $K_{p\_\omega\_\text{HIl}} = 0.12$, and $K_{i\_\omega\_\text{HIl}} = 0.72$.

### A. Complexity Level and Computational Burden

The computational time of algorithm implementation is one of the most important criteria, which are used to compare the complexity level of different control techniques. Since the computational time defines the type of the hardware required to implement the code; an increase of the computational time requires more expensive hardware controller and vice versa.

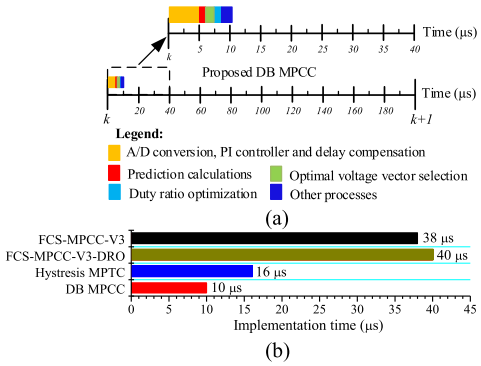


Fig. 16. Real time implementation by TMS320F28335 DSP. (a) Details of the proposed DB MPCC. (b) Comparison of the studied schemes.

Fig. 16 shows the code implementation time details of the proposed DB MPCC and compares the implementation time of the four algorithms.

The TMS320F28335 DSP requires 38 $\mu$s to implement the FCS-MPCC-V3 scheme due to the exploration process of all available V3. This time is increased by adding the duty ratio optimization to be 40 $\mu$s in the FCS-MPCC-V3-DRO algorithm. The hysteresis MPTC has reduced the exploration process from all available V3 to only two V3 during every control cycle. Hence, the implementation of the hysteresis MPTC is quite simpler, and it requires 16 $\mu$s to be implemented by the DSP. However, the proposed DB MPCC is implemented within only 10 $\mu$s, which is much smaller. This is because the proposed DB MPCC algorithm does not need any vector exploration process, in addition to there is no cost function evaluation. Hence, the proposed algorithm has the lowest computational burden, which is very important especially for multiphase or multilevel systems.

### *B. Steady-State Performance*

For further verification of the effectiveness of the proposed method, the steady-state HIL results of the proposed algorithm is compared with that of other studied control schemes, as shown in Fig. 17. The steady-state performance has been tested at a reference speed of 80 rad/s and a load torque of 15 N·m. Fig. 17 verifies that the current and the torque qualities in the proposed algorithm and the FCS-MPCC-V3-DRO are similar. Both algorithms exhibit the best performance among the studied algorithms. Fig. 18 shows a comparison of current FFT analysis of the studied control schemes. The current THD in the DB MPCC scheme (6.33%) is approximately similar to that of the FCS-MPCC-V3-DRO (6.26%). Both techniques have reduced current THD compared with the hysteresis MPTC (8.48%) and the FCS-MPCC-V3 (9.89%).

In addition, the proposed technique is compared with the studied control schemes at different sampling frequencies and different rotor speeds. The selected comparison criteria are the torque ripples and the current ripples. The torque ripples of the proposed DB MPCC are smaller than that of the hysteresis MPTC at all rotor speeds and sampling frequencies, as depicted by Fig. 19. Fig. 20 compares the current ripples of the studied

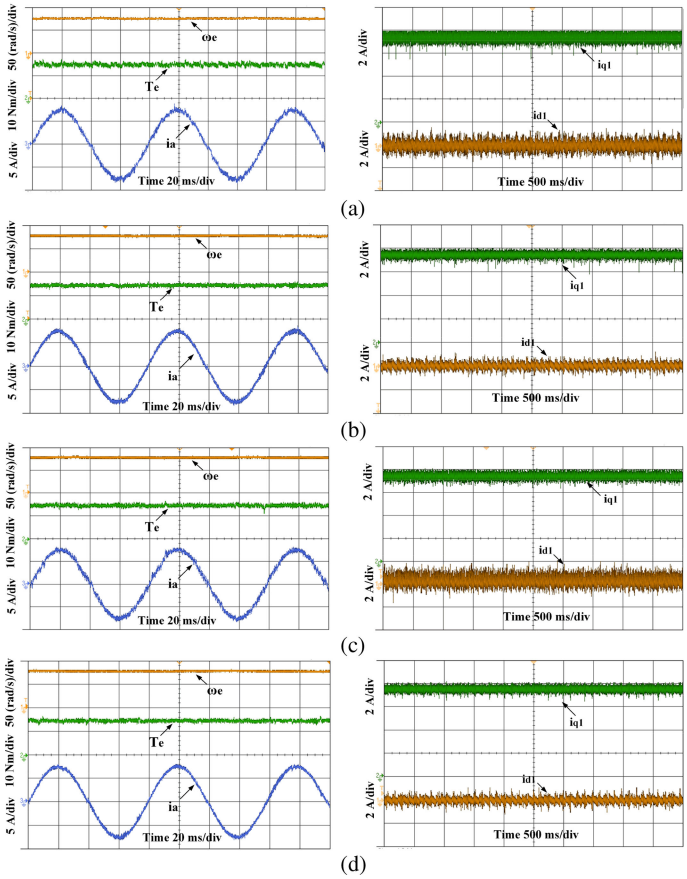


Fig. 17. Steady-state results comparison of (a) FCS-MPCC-V3. (b) FCS-MPCC-V3-DRO. (c) Hysteresis MPTC. (d) Proposed DB MPCC.

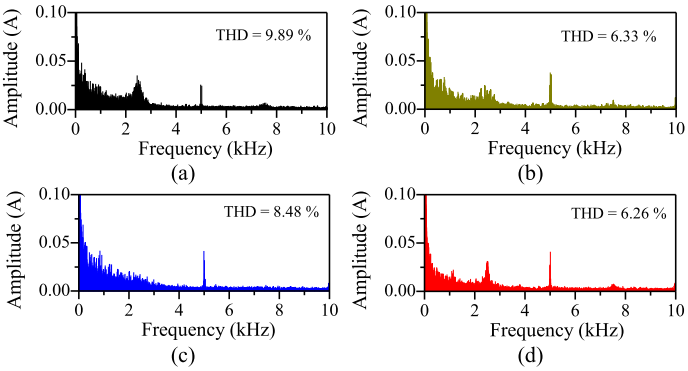


Fig. 18. FFT analysis of phase currents of (a) FCS-MPCC-V3. (b) FCS-MPCC-V3-DRO. (c) Hysteresis MPTC. (d) Proposed DB MPCC.

control schemes at a speed range from 10 to 80 rad/s. The *dq*-axes current ripples $i_{d\_r}$, $i_{q\_r}$, at $n$ data points, are calculated as follows:

$$\begin{cases} i_{d\_r} = \sqrt{\frac{1}{n}\sum_{i=1}^{n}\left(i_{\mathrm{d}\_i}\right)^2} \\ i_{q\_r} = \sqrt{\frac{1}{n}\sum_{i=1}^{n}\left(i_{q\_i}^{*} - i_{\mathrm{q}\_i}\right)^2}. \end{cases} \tag{39}$$

It can be seen from Fig. 20 that the proposed DB MPCC and the FCS-MPCC-V3-DRO exhibit approximately similar current ripples, which are lower than that of other strategies.

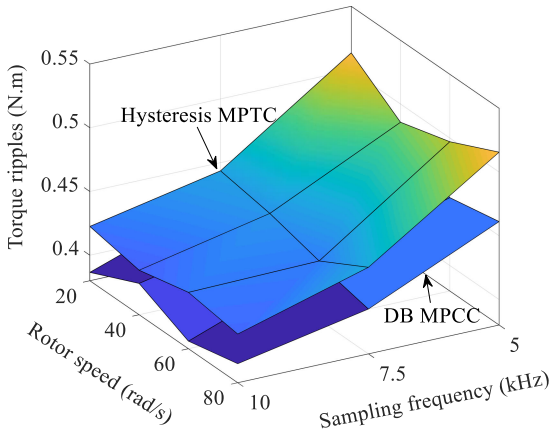


Fig. 19. Comparison of torque ripples between the proposed DB MPCC and the hysteresis MPTC at different sampling frequencies.

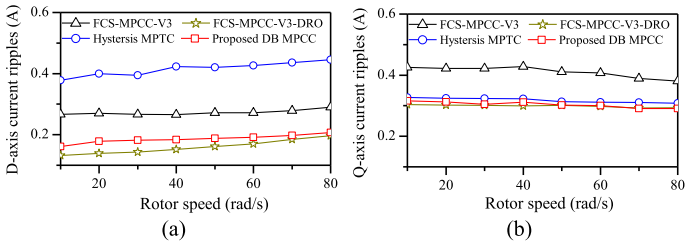


Fig. 20. Comparison of HIL current ripples. (a) $d$-axis current ripples. (b) $q$-axis current ripples.

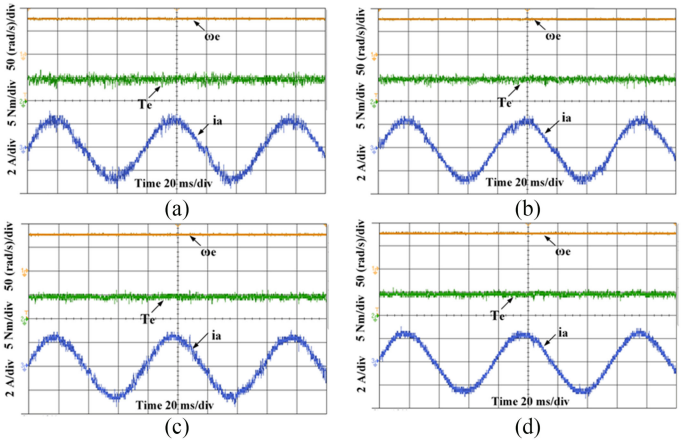


Fig. 21. HIL steady-state performance at 5 N·m load. (a) FCS-MPCC-V3. (b) FCS-MPCC-V3-DRO. (c) Hysteresis MPTC. (d) Proposed DB MPCC.

The hysteresis MPTC technique exhibits reduced $q$-axis current ripples, however, it has the highest $d$-axis current ripples. This is because the hysteresis MPTC algorithm considers only the torque error, hence, the $q$-axis current error, minimization in the duty ratio optimization.

A performance comparison of the four schemes under light load and low-speed conditions is validated and shown in Figs. 21 and 22, respectively. Fig. 21 shows the HIL results of the four schemes at 5 N·m load torque with sampling time of 100 $\mu$s. The HIL results verify the simulation results in that the FCS-MPCC-V3 scheme has the worst performance at the same sampling interval. Furthermore, the proposed control algorithm,

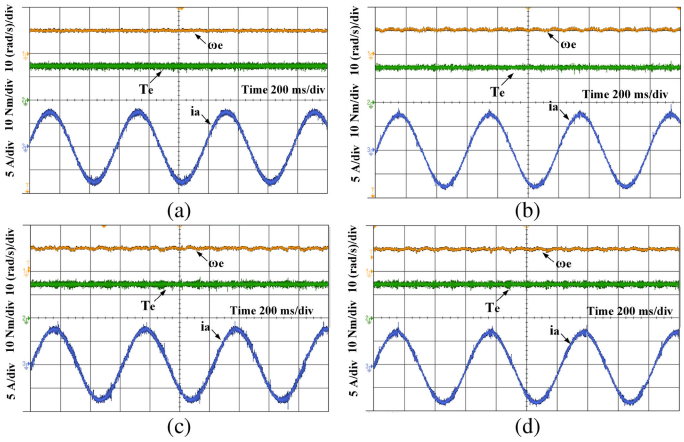


Fig. 22. HIL steady-state performance at 10 rad/s under nearly similar average switching frequency of 3.5 kHz. (a) FCS-MPCC-V3. (b) FCS-MPCC-V3-DRO. (c) Hysteresis MPTC. (d) Proposed DB MPCC.

TABLE VI
HIL RESULTS COMPARISON UNDER SIMILAR AVERAGE SWITCHING FREQUENCY

| | $F_{sw}$(kHz) | $T_s(\mu s)$ | $i_{d\_r}$ (A) | $i_{q\_r}$ (A) | $T_r(Nm)$ |
|---|---|---|---|---|---|
| FCS-MPCC-V3 | 3.58 | 100 | 0.176 | 0.200 | 0.504 |
| FCS-MPCC-V3-DRO | 3.54 | 200 | 0.196 | 0.157 | 0.434 |
| Hysteresis-MPTC | 3.47 | 200 | 0.405 | 0.192 | 0.516 |
| Proposed DB MPCC | 3.54 | 200 | 0.196 | 0.197 | 0.441 |

like FCS-MPCC-V3-DRO, exhibits the best steady-state performance among the studied algorithms. Under similar average switching frequency, the proposed DB MPCC still have the advantage over other control schemes at low and high-speed conditions, as depicted by Fig. 22 and Table VI, respectively.

### C. Dynamic Performance

Besides the steady-state performance, the dynamic performance of the proposed algorithm has been evaluated. The dynamic performance evaluation includes three different tests: load torque step change response, speed step change response, and speed reversal response. Fig. 23 shows the load torque step change response. The load torque steps up from 10 to 15 N·m at 0.25 s and steps down again from 15 to 10 N·m at 0.75 s. From Fig. 23, it can be noticed that all studied control schemes can achieve fast dynamic response for load changes, since the desired load torque can be achieved within around 10 ms. The load torque disturbance has a small effect on the rotor speed, which returns to its reference value quickly after the disturbance moment. Thus, these algorithms have the same robustness against the load torque disturbance.

The controller response to the rotor speed step change is compared for the studied schemes, as shown in Fig. 24. The rotor speed steps from zero to 80 rad/s. Although the proposed algorithm has the same load torque dynamic response as the hysteresis MPTC, its response to the speed step change, like other current control algorithms, is slightly slower than that of the MPTC, as depicted in Fig. 24. The hysteresis MPTC algorithm controls the electromagnetic torque directly, which

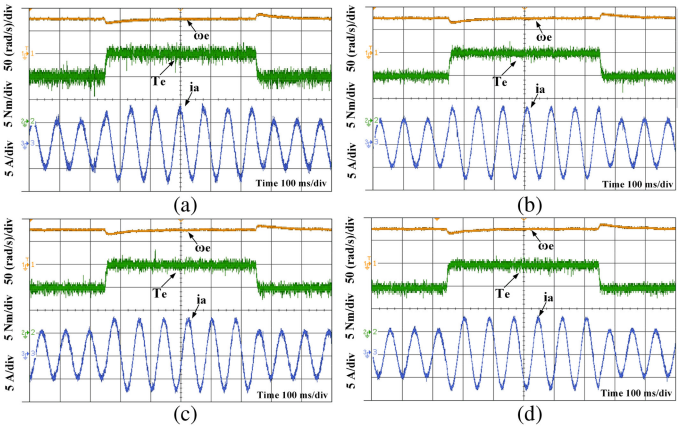


Fig. 23. Comparison of load torque disturbance response. (a) FCS-MPCC-V3. (b) FCS-MPCC-V3-DRO. (c) Hysteresis MPTC. (d) Proposed DB MPCC.

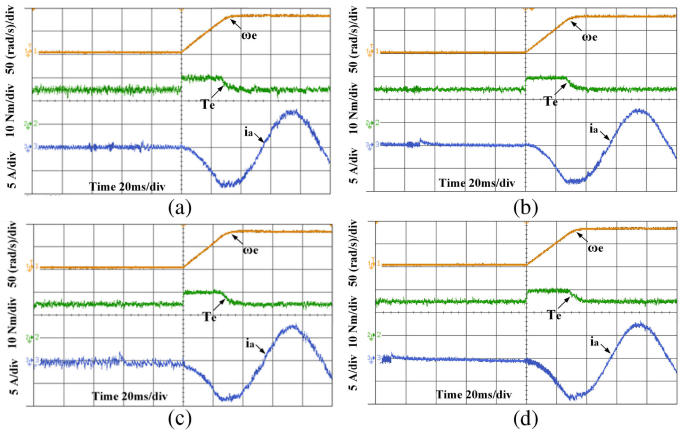


Fig. 24. Comparison of speed step change response. (a) FCS-MPCC-V3. (b) FCS-MPCC-V3-DRO. (c) Hysteresis MPTC. (d) Proposed DB MPCC.

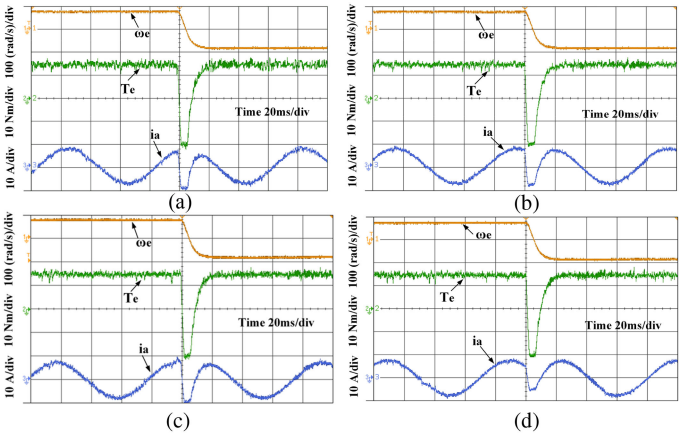


Fig. 25. Comparison of speed reversal response. (a) FCS-MPCC-V3. (b) FCS-MPCC-V3-DRO. (c) Hysteresis MPTC. (d) Proposed DB MPCC.

makes it faster than the proposed MPCC technique. However, the difference between the responses of both controller types is only few milliseconds. Fig. 25 compares the speed reversal response for the proposed DB MPCC and the other studied techniques. The motor was running first at 80 rad/s then the speed is reversed

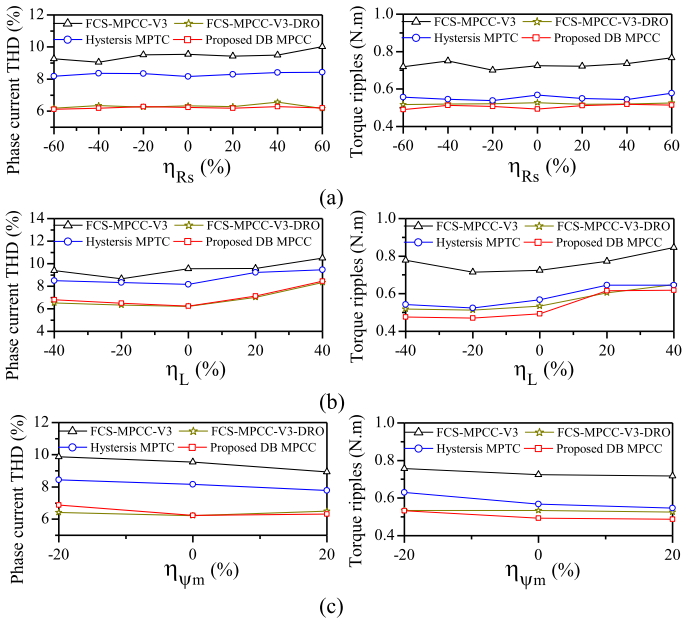


Fig. 26. Comparison of parameters mismatch sensitivity. (a) Resistance mismatch. (b) Inductance mismatch. (c) Rotor flux mismatch.

to −80 rad/s. It is clear that the speed reversal response is very fast for all algorithms with the aid of maximum negative torque, as shown in Fig. 25.

### *D. Sensitivity to Parameter's Mismatch*

The simulation and the HIL results have been taken with accurate machine parameters given to the controller. However, in real PMSM operation, the motor parameters may change during the operation. In PMSMs, the inductances of the machine may change during operation due to the saturation effects. In addition, the resistance of the machine changes with temperature variations. Moreover, the PM flux linkage may change if they are exposed to thermal or mechanical stresses. Therefore, it is important to investigate the operation of the proposed DB MPCC under parameter's mismatch. The effect of the parameter's mismatch on the control performance of the four studied methods is analyzed by considering the parameter mismatch ratio $\eta_x$, which is given as follows:

$$\eta_x = 1 - \frac{X}{X'} \tag{40}$$

where $X$ represents the actual parameter, while $X'$ is the mismatched parameter. The performance assessment criteria are chosen as the torque ripples, and the phase currents THD. Fig. 26 shows the effects of different parameters mismatch on the performances of the studied algorithms. The stator resistance and the rotor flux mismatches have unnoticeable effects on the control performance of these algorithms. However, the inductance mismatch slightly increases the harmonics and the ripples of all studied algorithms. Fortunately, the proposed DB MPCC technique, is similar to the FCS-MPCC-V3-DRO, still have reduced ripples and harmonics at different inductance mismatch ratios, as shown in Fig. 26.

TABLE VII
HIL RESULTS COMPARISON OF THE PROPOSED CONTROL SCHEME WITH EXISTING CONTROL TECHNIQUES

| | Steady-state harmonics | Dynamic response | Computational time | Switching frequency |
|---|---|---|---|---|
| PI-CBPWM | lowest | slow | low (27 μs) | constant |
| FCS-MPCC31 | moderate | fast | very high (82 μs) | variable |
| FCS-MPCC21 | high | moderate | high (57 μs) | variable |
| FCS-MPCC11 | high | moderate | moderate (36 μs) | variable |
| FCS-MPCC-V3 | moderate | fast | moderate (38 μs) | nearly constant |
| FCS-MPCC-V3-DRO | very low | fast | moderate (40 μs) | constant |
| Hysteresis-MPTC | low | fastest | low (16 μs) | constant |
| Proposed DB MPCC | very low | fast | lowest (10 μs) | constant |

### *E. Overall Performance Evaluation of the Proposed Control Scheme*

In order to guarantee a clear and fair evaluation of the proposed algorithm, a comprehensive comparison of the proposed algorithm with the existing algorithms is listed in Table VII. The predictive control techniques have the salient advantages of fast dynamic response, nonlinearity consideration, compared with traditional methods such as PI-CBPWM. In contrast, the PI-CBPWM has the advantages of lowest harmonics, constant switching frequency, and relatively low computational burden. However, the proposed DB MPCC combines some advantages of both types of controllers. Since it has fast dynamic response, nonlinearity consideration, relatively low harmonics, and constant switching frequency. Furthermore, the proposed algorithm has the lowest computational burden among all existing control schemes.

## VII. CONCLUSION

This article introduces a low-complexity DB MPCC algorithm for five-phase PMSM drives. The proposed technique uses the DB control principles to calculate the reference voltage vector. From this information, the optimal voltage vector is directly selected from the enhanced control-set, which eliminates the third harmonic components. Therefore, the computational burden can be significantly reduced. In addition, a duty ratio optimization is used in the proposed method to improve the steady-state performance. The simulation and HIL results show that the proposed control scheme combines the advantages of the existing control schemes. Compared with existing control schemes applied on five-phase drive systems, the proposed scheme has the following salient features.

1) There is no cost function evaluation and no exploration processes.
2) The proposed scheme has the lowest computational time of 10 $\mu$s compared with the existing control schemes. This feature reduces the hardware implementation cost of the algorithm, especially for multiphase and multilevel drive systems.
3) Similar to the FCS-MPCC-V3-DRO algorithm, the proposed scheme presents a superior steady-state performance compared with the conventional MPC-based schemes under similar average switching frequency.
4) The duty-ratio calculation of the proposed scheme is considered as the general form compared with the existing algorithms.
5) Like other MPC schemes, the proposed DB MPCC has a fast response to the rotor speed step change, although it exhibits slightly slower speed compared with the hysteresis MPTC.

## REFERENCES

[1] E. Levi, R. Bojoi, F. Profumo, H. Toliyat, and S. Williamson, "Multiphase induction motor drives–A technology status review," *IET Electr. Power Appl.*, vol. 1, pp. 489–516, Jul. 2007.
[2] E. Levi, "Multiphase electric machines for variable-speed applications," *IEEE Trans. Ind. Electron*, vol. 55, no. 5, pp. 1893–1909, May 2008.
[3] L. Parsa and H. A. Toliyat, "Sensorless direct torque control of five-phase interior permanent-magnet motor drives," *IEEE Trans. Ind. Appl.*, vol. 43, no. 4, pp. 952–959, Jul./Aug. 2007.
[4] C. Liang, J.-C. Le Claire, M. Aït-Ahmed, and M.-F. Benkhoris, "Power control of 5-phase PMSG-diode rectifier-interleaved Boost set under health and fault modes," *Electr. Power Syst. Res.*, vol. 152, pp. 316–322, Nov. 2017.
[5] H. H. Mousa, A.-R. Youssef, and E. E. Mohamed, "Variable step size P&O MPPT algorithm for optimal power extraction of multi-phase PMSG based wind generation system," *Electr. Power Energy Syst.*, vol. 108, pp. 218–231, Jun. 2019.
[6] S. Vazquez, J. Rodriguez, M. Rivera, L. G. Franquelo, and M. Norambuena, "Model predictive control for power converters and drives: Advances and trends," *IEEE Trans. Ind. Electron*, vol. 64, no. 2, pp. 935–947, Feb. 2017.
[7] H. Abu-Rub, J. Guzinski, Z. Krzeminski, and H. A. Toliyat, "Predictive current control of voltage-source inverters," *IEEE Trans. Ind. Electron.*, vol. 51, no. 3, pp. 585–593, Jun. 2004.
[8] T. Geyer, G. Papafotiou, and M. Morari, "Model predictive direct torque control—Part I: Concept, algorithm, and analysis," *IEEE Trans. Ind. Electron*, vol. 56, no. 6, pp. 1894–1905, Jun. 2009.
[9] H. Miranda, P. Cortés, J. I. Yuz, and J. Rodríguez, "Predictive torque control of induction machines based on state-space models," *IEEE Trans. Ind. Electron*, vol. 56, no. 6, pp. 1916–1924, Jun. 2009.
[10] S. Kouro, P. Cortés, R. Vargas, U. Ammann, and J. Rodríguez, "Model predictive control—A simple and powerful method to control power converters," *IEEE Trans. Ind. Electron*, vol. 56, no. 6, pp. 1826–1838, Jun. 2009.
[11] C. S. Lim, E. Levi, M. Jones, N. A. Rahim, and W. P. Hew, "FCS-MPC-Based current control of a five-phase induction motor and its comparison with PI-PWM control," *IEEE Trans. Ind. Electron*, vol. 61, no. 1, pp. 149–163, Jan. 2014.
[12] P. Cortés, M. P. Kazmierkowski, R. M. Kennel, D. E. Quevedo, and J. Rodríguez, "Predictive control in power electronics and drives," *IEEE Trans. Ind. Electron*, vol. 55, no. 12, pp. 4312–4324, Dec. 2008.
[13] M. A. Perez, J. Rodriguez, E. J. Fuentes, and F. Kammerer, "Predictive control of AC–AC modular multilevel converters," *IEEE Trans. Ind. Electron*, vol. 59, no. 7, pp. 2832–2839, Jul. 2012.
[14] F. Donoso, A. Mora, R. Cárdenas, A. Angulo, D. Sáez, and M. Rivera, "Finite-set model-predictive control strategies for a 3L-NPC inverter operating with fixed switching frequency," *IEEE Trans. Ind. Electron*, vol. 65, no. 5, pp. 3954–3965, May 2018.
[15] L. Tarisciotti, P. Zanchetta, A. Watson, J. Clare, M. Degano, and S. Bifaretti, "Modulated model predictive control for a three-phase active rectifier," *IEEE Trans. Ind. Appl.*, vol. 51, no. 2, pp. 1610–1620, Mar./Apr. 2015.
[16] R. Baidya, R. P. Aguilera, P. Acuna, S. Vazquez, and H. du Toit Mouton, "Multistep model predictive control for cascaded h-bridge inverters: Formulation and analysis," *IEEE Trans. Power Electron*, vol. 33, no. 1, pp. 876–886, Jan. 2018.
[17] T. Geyer and D. E. Quevedo, "Multistep finite control set model predictive control for power electronics," *IEEE Trans. Power Electron.*, vol. 29, no. 12, pp. 6836–6846, Dec. 2014.
[18] L. Tarisciotti, P. Zanchetta, A. Watson, S. Bifaretti, and J. C. Clare, "Modulated model predictive control for a seven-level cascaded H-bridge back-to-back converter," *IEEE Trans. Ind. Electron.*, vol. 61, no. 10, pp. 5375–5383, Oct. 2014.
[19] M. Vijayagopal, P. Zanchetta, L. Empringham, L. De Lillo, L. Tarisciotti, and P. Wheeler, "Control of a direct matrix converter with modulated model-predictive control," *IEEE Trans. Ind. Appl.*, vol. 53, no. 3, pp. 2342–2349, May/Jun. 2017.

[20] H. Mahmoudi, M. Aleenejad, and R. Ahmadi, "A new multiobjective modulated model predictive control method with adaptive objective prioritization," *IEEE Trans. Ind. Appl.*, vol. 53, no. 2, pp. 1188–1199, Mar./Apr. 2017.
[21] Z. He, P. Guo, Z. Shuai, Q. Xu, A. Luo, and J. M. Guerrero, "Modulated model predictive control for modular multilevel AC/AC converter," *IEEE Trans. Power Electron*, vol. 34, no. 10, pp. 10359–10372, Oct. 2019.
[22] S. Vazquez *et al.*, "Model predictive control for single-phase NPC converters based on optimal switching sequences," *IEEE Trans. Ind. Electron*, vol. 63, no. 12, pp. 7533–7541, Dec. 2016.
[23] S. Vázquez Pérez *et al.*, "Model predictive control with constant switching frequency using a discrete space vector modulation with virtual state vectors," in *Proc. Int. Conf. Ind. Tech.*, 2009, pp. 1–6.
[24] C. Xue, W. Song, and X. Feng, "Finite control-set model predictive current control of five-phase permanent-magnet synchronous machine based on virtual voltage vectors," *IET Electr. Power Appl.*, vol. 11, pp. 836–846, 2017.
[25] Y. Ren and Z. Q. Zhu, "Reduction of both harmonic current and torque ripple for dual three-phase permanent-magnet synchronous machine using modified switching-table-based direct torque control," *IEEE Trans. Ind. Electron*, vol. 62, no. 11, pp. 6671–6683, Nov. 2015.
[26] C. Xue, W. Song, X. Wu, and X. Feng, "A constant switching frequency finite-control-set predictive current control scheme of a five-phase inverter with duty-ratio optimization," *IEEE Trans. Power Electron.*, vol. 33, no. 4, pp. 3583–3594, Apr. 2018.
[27] Y. Zhang and H. Lin, "Simplified model predictive current control method of voltage-source inverter," in *Proc. 8th Int. Conf. on Power Electron*, 2011, pp. 1726–1733.
[28] Y. Zhang, L. Huang, D. Xu, J. Liu, and J. Jin, "Performance evaluation of two-vector-based model predictive current control of PMSM drives," *Chin. J. Elect. Eng.*, vol. 4, pp. 65–81, Jun. 2018.
[29] Y. Zhang and H. Yang, "Two-vector-based model predictive torque control without weighting factors for induction motor drives," *IEEE Trans. Power Electron.*, vol. 31, no. 2, pp. 1381–1390, Feb. 2016.
[30] S. Kang, J. Soh, and R. Kim, "Symmetrical three-vector-based model predictive control with deadbeat solution for IPMSM in rotating reference frame," *IEEE Trans. Ind. Electron*, vol. 67, no. 1, pp. 159–168, Jan. 2020.
[31] Y. Zhang, D. Xu, and L. Huang, "Generalized multiple-vector-based model predictive control for PMSM drives," *IEEE Trans. Ind. Electron*, vol. 65, no. 12, pp. 9356–9366, Dec. 2018.
[32] Y. Zhang, Y. Bai and H. Yang, "A universal multiple-vector-based model predictive control of induction motor drives," *IEEE Trans. Ind. Electron*, vol. 33, no. 8, pp. 6957–6969, Aug. 2018.
[33] W. Xie *et al.*, "Finite-control-set model predictive torque control with a deadbeat solution for PMSM drives," *IEEE Trans. Ind. Electron*, vol. 62, no. 9, pp. 5402–5410, Sep. 2015.
[34] M. Norambuena *et al.*, "A very simple strategy for high-quality performance of AC machines using model predictive control," *IEEE Trans. Power Electron.*, vol. 34, no. 1, pp. 794–800, Jan. 2019.
[35] P. Cortes, A. Wilson, S. Kouro, J. Rodriguez, and H. Abu-Rub, "Model predictive control of multilevel cascaded H-bridge inverters," *IEEE Trans. Ind. Electron.*, vol. 57, no. 8, pp. 2691–2699, Aug. 2010.
[36] C. Xiong, H. Xu, T. Guan, and P. Zhou, "A constant switching frequency multiple-vector-based model predictive current control of five-phase PMSM with nonsinusoidal back EMF," *IEEE Trans. Ind. Electron*, vol. 67, no. 3, pp. 1695–1707, Mar. 2020.
[37] Y. Luo and C. Liu, "Multi-vector-based model predictive torque control for a six-phase PMSM motor with fixed switching frequency," *IEEE Trans. Energy Convers*, vol. 34, no. 3, pp. 1369–1379, Sep. 2019.
[38] G. Li, J. Hu, Y. Li and J. Zhu, "An improved model predictive direct torque control strategy for reducing harmonic currents and torque ripples of five-phase permanent magnet synchronous motors," *IEEE Trans. Ind. Electron*, vol. 66, no. 8, pp. 5820–5829, Aug. 2019.
[39] X. Wu, W. Song, and C. Xue, "Low-complexity model predictive torque control method without weighting factor for five-phase PMSM based on hysteresis comparators," *IEEE J. Emerg. Select. Topics Power Electron.*, vol. 6, no. 4, pp. 1650–1661, Dec. 2018.
[40] F. Barrero, M. R. Arahal, R. Gregor, S. Toral, and M. J. Durán, "A proof of concept study of predictive current control for VSI-driven asymmetrical dual three-phase AC machines," *IEEE Trans. Ind. Electron.*, vol. 56, no. 6, pp. 1937–1954, Jun. 2009.
[41] C. S. Lim, N. Rahim, W. Hew, M. Jones, and E. Levi, "Model predictive current control of a five-phase induction motor," in *Proc. IECON-37th IEEE Annu. Conf. Ind. Electron. Soc.*, 2011, pp. 1934–1940.
[42] P. Karamanakos, and T. Geyer, "Guidelines for the design of finite control set model predictive controllers," *IEEE Trans. Power. Electron.*, vol. 35, no. 7, pp. 7434–7450, Jul. 2020.
[43] T. Kawabata, T. Miyashita, and Y. Yamamoto, "Dead beat control of three phase PWM inverter," *IEEE Trans. Power Electron.*, vol. 5, no. 1, pp. 21–28, Jan. 1990.
[44] L. Malesani, P. Mattavelli, and S. Buso, "Robust dead-beat current control for PWM rectifiers and active filters," *IEEE Trans. Ind. Appl.*, vol. 35, no. 3, pp. 613–620, May/Jun. 1999.
[45] S. Yang and K. Lin, "Automatic control loop tuning for permanent-magnet AC servo motor drives," *IEEE Trans. Ind. Electron.*, vol. 63, no. 3, pp. 1499–1506, Mar. 2016.
[46] H. Lei, "Inertia identification and PI parameter tuning of PMSM servo drives," in *Proc. IOP Conf. Series: Materials Sci. Eng.*, 2017, Art. no. 012117.

**Mahmoud S. R. Saeed** was born in Qena, Egypt, in 1991. He received the B.S. and M.S. degrees in electrical power and machines engineering from the Faculty of Engineering, South Valley University, Qena, Egypt, in 2013 and 2018, respectively. He is currently working toward the Ph.D. degree with Southwest Jiaotong University, Chengdu, China.

Since 2015, he joined as an Administrator with the Department of Electrical Engineering, Faculty of Engineering, South Valley University, Qena, Egypt, a Research Assistant since 2018, and then, as an Assistant Lecturer. His research interests include electrical machines design and control, power electronics and drive systems, and renewable energy systems.

**Wensheng Song** (Member, IEEE) received the B.S. degree in electronic and information engineering and the Ph.D. degree in electrical engineering from Southwest Jiaotong University, Chengdu, China, in 2006 and 2011, respectively.

He is currently a Full Professor with the School of Electrical Engineering, Southwest Jiaotong University. From 2009 to 2010, he was a Visiting Scholar with the Department of Electrical Engineering and Computer Science, University of California, Irvine, CA, USA. From July 2015 to December 2015, he was a Visiting Scholar with University of Alberta, Edmonton, AB, Canada. His current research interests include railway electric traction drive systems, high power energy conversion, power electronic transformers, and predictive control.

**Bin Yu** was born in Chengdu, China, in 1991. He received the B.S. degree in electrical engineering in 2015 from Southwest Jiaotong University, Chengdu, China, where he is currently working toward the Ph.D. degree in electrical engineering.

His current research interests include power electronics and multiphase machine drives.

**Xuesong Wu** was born in Anhui, China, in 1994. He received the B.S. and M.S. degree in electrical engineering from Southwest Jiaotong University, Chengdu, China, in 2016 and 2019, respectively. He is currently toward the Ph.D. degree with the University of Alberta, Edmonton, AB, Canada.

His current research interests include motor drive and predictive control.